water

MDPI

Article

Validation of Sea Level Anomalies from the SWOT Altimetry Mission Around the Coastal Regions of East Asia and the US West Coast

Haojie Zhu [1], Fukai Peng [2,*] and Yunzhong Shen [1]

[1] College of Surveying and Geo-Informatics, Tongji University, Shanghai 200092, China
[2] School of Geospatial Engineering and Science, Sun Yat-sen University, Zhuhai 510275, China
* Correspondence: pengfk@mail.sysu.edu.cn

Abstract

The validation of altimeter data in the coastal zones is of great importance for monitoring coastal sea level changes. Therefore, this study focuses on the validation of sea level anomaly (*SLA*) estimates from three altimetry missions (i.e., SWOT, ICESat-2 and Sentinel-3A) within the distance band of 50 km to the coast in two study areas: the coastal region of East Asia (0° N–40° N, 100° E–140° E) and the US West Coast (30° N–60° N, 145° W–115° W). The selection of these three missions is because they carry the advanced radar and laser altimeters. Although the validation of any single altimeter is not new, the comparison of their performance together in the coastal zones is the first time to our knowledge. Because the spatial resolutions of these three altimeters are different, the spatially averaged altimeter measurements are used for the validation against tide gauges. Moreover, the validation is conducted over four coastal strips (0–5 km, 5–10 km, 10–20 km, and 20–50 km) to better reveal their performance when approaching towards the coastlines. The results show that these three missions achieve similar performance in terms of correlation coefficient and Root Mean Square Error (RMSE) in the 5–50 km coastal strip. The superior performance of the SWOT mission to the ICESat-2 and Sentinel-3A is observed in the last 5 km to coasts (0.06 m/0.73 against 0.09 m/0.70 and 0.12 m/0.63 for coastal regions of East Asia, 0.11 m/0.79 against 0.10 m/0.82 and 0.14 m/0.72 for the US West Coast), where the land contamination is the most significant. The ICESat-2 achieves the best performance (0.10 m) in the US West Coast due to the reduced range bias in higher latitudes, and the SWOT outperforms in the lower-latitude East Asia coastal region (0.06 m). To further investigate the data quality of the SWOT mission, a triple collocation model is applied to quantify the errors. The results reveal that the SWOT obtains similar error variance relative to the tide gauges in both study areas (i.e., 0.010 m^2 vs. 0.005 m^2 for the coastal region of East Asia, and 0.010 m^2 vs. 0.007 m^2 for the US West Coast). The above findings highlight the SWOT's advantages in monitoring the coastal sea level changes.

Keywords: SWOT; satellite altimetry; tide gauges; sea level anomaly; validation

check for updates

Academic Editor: Paul Kucera

Received: 25 September 2025
Revised: 20 October 2025
Accepted: 20 October 2025
Published: 26 October 2025

Citation: Zhu, H.; Peng, F.; Shen, Y. Validation of Sea Level Anomalies from the SWOT Altimetry Mission Around the Coastal Regions of East Asia and the US West Coast. *Water* **2025**, *17*, 3066. https://doi.org/10.3390/w17213066

Copyright: © 2025 by the authors. Licensee MDPI, Basel, Switzerland. This article is an open access article distributed under the terms and conditions of the Creative Commons Attribution (CC BY) license (https://creativecommons.org/licenses/by/4.0/).

1. Introduction

In the context of global climate change, sea level rise has become a critical environmental issue, which results in increasing threats to coastal infrastructure, ecosystems, and human settlements [1,2]. Accurate and long-term monitoring of sea surface height (SSH) data is therefore essential for climate studies, flood risk assessment, and shipping. Traditionally, although tide gauges have served as the primary source for SSH observations [3–6],

their sparse and uneven distribution limit their ability to capture large-scale SSH variability. As a crucial supplement, satellite altimeters provide broader spatial coverage and consistent SSH measurements over global oceans. During the last few decades, numerous altimetry missions have reached a high level of maturity in marine applications, providing ocean products with unprecedented accuracy [7,8]. Unfortunately, as satellite altimeters approach the coast, data quality often degrades due to factors such as inaccurate corrections and land contamination of radar returns [9,10]. To address these problems, new-generation altimetry satellites (i.e., Sentinel-3A, ICESat-2, and SWOT) with finer spatial resolutions and enhanced measurement accuracy have been developed and have the potential to substantially improve our understanding of sea level variations near the coast. However, the availability and accuracy of their observations in coastal regions have not been systematically assessed together. Therefore, this study focuses on evaluating the performance of Sentinel-3A, ICESat-2, and SWOT data in two coastal areas. These regions are selected because they differ significantly in latitude and oceanographic conditions, providing a valuable contrast for assessing altimetry performance in different latitude bands.

Sentinel-3A is the first satellite altimeter to provide global ocean observations in Synthetic Aperture Radar (SAR) mode [11]. The altimeter emits high-frequency pulse bursts (17.8 kHz) to perform coherent signal processing and applies Delay-Doppler processing to enhance measurement precision and spatial resolution. Specifically, a Fast Fourier Transform (FFT) is applied to the pulses within each burst, separating the return signals into distinct Doppler beams. Each Doppler strip (approximately 330 m wide in the along-track direction) is sampled repeatedly over a time window of about 2.5 s as the satellite moves forward, which enables multiple observations of the same location from different positions [12]. These observations are then coherently combined in a process known as stacking, which reduces the speckle noise and improves the signal-to-noise ratio. The Sentinel-3A SAR mode data have been validated in various regions, and these findings consistently indicate that its measurements show improved performance in the open ocean environments [13–15]. However, its across-track footprint remains relatively large (~2–7 km), which is a limitation that has not been mitigated. Recent studies have also shown that its performance degrades when the satellite track runs parallel and close to the coastline, primarily due to increased land contamination from the across-track direction [16].

The Ice, Cloud, and land Elevation Satellite-2 (ICESat-2), which was launched in September 2018, expands spatial coverage up to 88° latitude. Equipped with the ATLAS (Advanced Topographic Laser Altimeter System) instrument, this satellite measures SSH by emitting green laser (532 nm) at a rate of 10,000 pulses per second, enabling an along-track sampling interval of ~0.7 m [17]. The altimeter is characterized by six laser beams arranged in three pairs separated by 3.3 km, with each pair comprising a strong and weak beam offset by approximately 90 m, which offers more redundant and detailed sampling near the reference ground track (RGT). In addition, a notable strength of ICESat-2 is its exceptionally small footprint (i.e., roughly 13 m to 17 m in diameter), which makes it highly effective for providing valid SSH data in coastal regions with less contamination from land [18]. These advantages have been demonstrated by the higher data availability of ICESat-2 significantly improves the accuracy of mean sea surface (MSS) in complex coastal environments [19]. However, several simulations demonstrated that the range bias errors increase at lower latitudes due to decreased crossover observations, which indicates the importance of evaluating the performance of ICESat-2 across regions with different latitudes [20].

The Surface Water and Ocean Topography (SWOT) mission was successfully launched in December 2022 to provide two-dimensional SSH measurements, enabling the observations of ocean features with wavelengths down to 15 km, unlike conventional altimetry satellites that observe only along narrow ground tracks [21]. The core of SWOT's innovative measurement system is the Ka-band Radar Interferometer (KaRIn), which consists of two synthetic aperture radar (SAR) antennas separated by a 10 m baseline. By receiving radar echoes from two slightly different perspectives, KaRIn forms two parallel swaths, each extending up to 60 km from the nadir, resulting in a total swath width of approximately 120 km. The 20 km gap in the center is sampled by a conventional Ku- and C-band altimeter, which enables broader spatial coverage and higher spatial resolution [22]. In addition to its spatial advantage, SWOT also features a revisit time that varies with different latitudes, providing a relatively dense temporal sampling at mid- to high-latitude [23]. Recent studies have confirmed the potential of SWOT for coastal studies, which demonstrates that the SWOT can successfully retrieve high-resolution SSH information in complex environments (e.g., estuaries and river deltas) where conventional nadir altimeters still have great challenges [21]. Therefore, it is of great interest to further quantify the data accuracy of SWOT in the coastal zones.

This paper is thus focused on the validation of sea level anomaly (*SLA*) observed by the three altimetry missions (i.e., Sentinel-3A, ICESat-2, and SWOT) over two coastal regions. The hourly tide gauge data from the University of Hawaii Sea Level Center (UHSLC) are used to validate the accuracy of satellite observations over the same time span. Furthermore, a triple collocation statistical model is applied to separate and quantify the errors of Sentinel-3A, ICESat-2, SWOT, and tide gauge data, respectively. The rest of the paper is structured as follows. Section 2 describes the study areas. Section 3 presents the datasets and validation methodology. Section 4 discusses the validation results, and Section 5 concludes key findings of this study.

2. Study Areas

2.1. The Coastal Region of East Asia

The coastal region of East Asia (0° N–40° N, 100° E–140° E), which is located in the eastern part of Eurasia, is part of the marginal seas of the northwestern Pacific (Figure 1). This area includes the Bohai Sea, Yellow Sea, East China Sea, and South China Sea, which is highly sensitive to climate and hydrological factors, such as the East Asian Monsoon, El Niño-Southern Oscillation (ENSO), runoff, and vertical land motion (VLM) [24–26]. These environmental drivers play an important role in sea level rise, which has been particularly pronounced in the last few decades.

The rate of sea level rise around Chinese coasts has reached 3.9 mm/yr, exceeding the global mean sea level rise (GMSL) during 1993–2020 [27]. Other parts of the study region have shown similar or even more pronounced trends (e.g., 3.6 mm/yr in Vietnam between 1993 and 2018 [28], 3.4 mm/yr around Japan from 2006 to 2018 [29]). Particularly rapid rates have been recorded in the Philippines, where sea level rose by 14.7 $\pm$ 4.39 mm/yr during 2002–2015 [30].

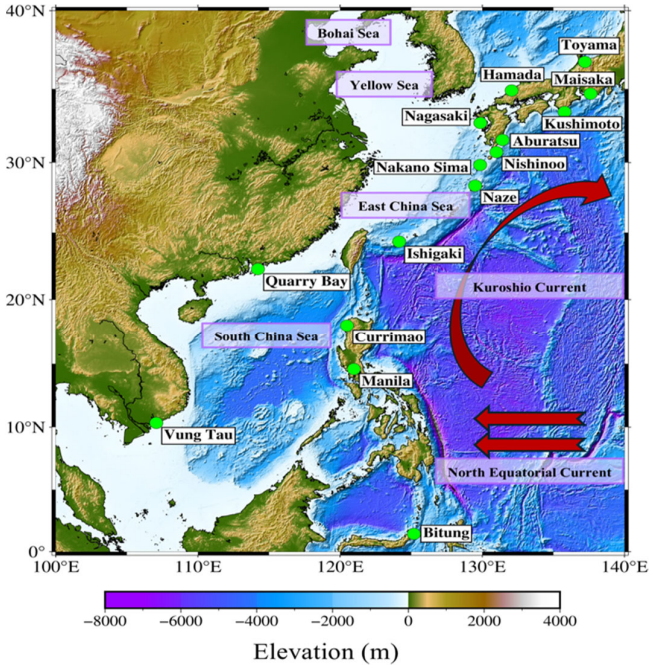


Figure 1. Distribution of tide gauges in the coastal region of East Asia. The solid green circles indicate the location of tide gauges. The color bar shows the bathymetry in the study area. The red arrows denote the main ocean currents in the region, including the Kuroshio Current and the North Equatorial Current.

2.2. The US West Coast

To investigate whether the performance of satellite altimeters would vary with different latitude bands, we also select the US West Coast (30° N–60° N, 145° W–115° W) as a comparative study region, which borders the North Pacific Ocean and extends to the Gulf of Alaska. This area is influenced by the large-scale ocean circulations (e.g., the North Pacific Current and the Alaska Current) (Figure 2), and presents distinct sea level characteristics influenced by both geological and climatic factors [31,32]. For instance, in the Gulf of Alaska, despite ongoing global sea level rise, local relative sea levels have declined in some areas due to land uplift caused by the Glacial Isostatic Adjustment (GIA), which is a process where the land continues to rebound following the retreat of ancient ice sheets [33]. In contrast, much of the US West Coast, which lacks such glacial history, is experiencing relative sea level rise that is closer to the global average. Additionally, during El Niño events, changes in wind patterns and ocean heat distribution raise coastal sea levels along the US West Coast, while La Niña tends to have the opposite effect [34]. Owing to its complex coastal terrain (including numerous fjords and islands) and the availability of sufficient tide gauge records, this region provides an ideal environment for validating altimetry data and examining performance across different latitude bands.

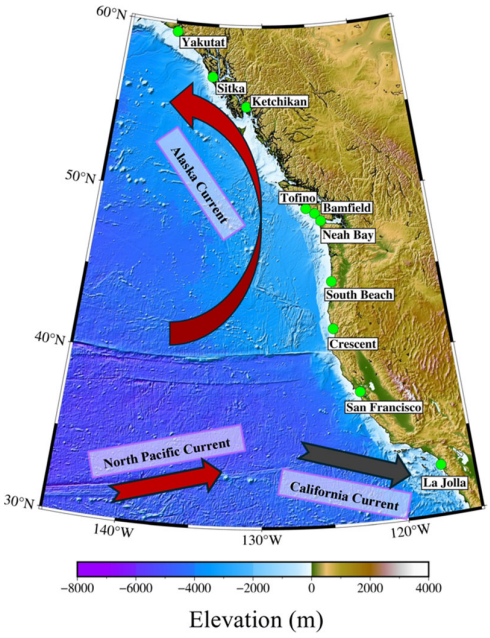


Figure 2. Distribution of tide gauges in the US West Coast. The solid green circles indicate the location of tide gauges. The color bar shows the bathymetry in the study area. This region includes both open ocean and continental shelf environments, such as the Gulf of Alaska. The red and gray arrows denote the major ocean currents in the region, including the Alaska Current, the North Pacific Current, and the California Current.

3. Materials and Methods

3.1. Datasets

Two data sources are used in this study. Firstly, SSH observations are derived from Sentinel-3A (cycles 37–121), ICESat-2 (cycles 1–25), and SWOT (cycles 1–26) missions. Secondly, tide gauge records are obtained from the UHSLC over the time period from October 2018 to December 2024. Table 1 summarizes the key technical parameters of these three satellites.

Table 1. Key technical parameters of Sentinel-3A, ICESat-2, and SWOT missions.

Mission	Reference Ellipsoid	Time Period	Repeat Cycles	Altimeter	Inclination	Sampling Interval
Sentinel-3A	WGS84	Oct 2018–Dec 2024	~27 days	SRAL	98.65°	~330 m
ICESat-2	WGS84	Oct 2018–Nov 2024	~91 days	ATLAS	92°	70 m–7 km
SWOT	WGS84	Jul 2023–Dec 2024	~21 days	KaRIn	77.6°	2 × 2 km

3.1.1. Sentinel-3A Data

Sentinel-3A carries the SAR Radar Altimeter (SRAL), which operates in a 27-day repeat cycle and provides SSH measurements from a sun-synchronous polar orbit. In this study, we use the SRAL Level 2 enhanced NTC (Non-Time Critical) product (version BC005) over the period from 14 October 2018 to 31 December 2024 (https://dataspace.copernicus.eu/ (accessed on 4 January 2025)), which provides detailed along-track measurements suitable for oceanographic applications at both 20 Hz and 1 Hz sampling rates. To obtain the 20 Hz *SLA*, we extract 20 Hz altitude, 20 Hz range measurements, 20 Hz MSS, 1 Hz range and geophysical corrections. The 1 Hz corrections are interpolated into the 20 Hz data using a nearest-neighbor method and subsequently applied to the 20 Hz range measurements.

Because these corrections show small variability at the spatial scales of several kilometers over ocean, the interpolation of 1 Hz corrections into 20 Hz corrections with adequate accuracy [35].

3.1.2. ICESat-2 Data

We utilize the ICESat-2 ocean product ATL12 (Version 6) spanning the period from 14 October 2018 to 8 November 2024, which can be accessed from the National Snow and Ice Data Center (NSIDC) (https://nsidc.org/data (accessed on 4 January 2025)). The ATL12 product includes SSH data derived exclusively from the strong beams due to the high reflectivity of the sea surface [36], with various corrections and quality flags, facilitating the calculation of *SLA* for further analysis in this study.

3.1.3. SWOT Data

We use the Level 3 SSH expert product (Version 1.0.2), which can be accessed from a registered account of the AVISO+ (Archiving, Validation and Interpretation of Satellite Oceanographic data plus) via ftp.aviso.altimetry.fr. The dataset corresponds to the SWOT science orbit phase, spanning from 26 July 2023 to 31 December 2024. Similarly, this product not only includes SSH data but also provides associated quality flags, range, and geophysical corrections [37]. Although the Level-3 product integrates data from multiple Level-2 product versions (PGC0, PIC0, and PIC2), these have been harmonized and quality-controlled within the L3 processing, ensuring consistency across cycles and minimizing the impact of version differences on our analysis.

3.1.4. Tide Gauge Data

The fast delivery tide gauge data provided by the UHSLC are used to validate the altimeter data. The tide gauge data can be accessed from the anonymous FTP account via ftp.soest.hawaii.edu. For validation in the coastal area of East Asia, we use the data from 15 tide gauges (Figure 1). For the US west coastal region, data from 10 tide gauges (Figure 2) are employed. The basic information for each tide gauge station, which includes longitude, latitude, time span, and data missing rate, is provided in Table 2.

Table 2. Summarized information of tide gauges used in this study.

Tide Gauge	Country	Location		Time Period	Missing Percentage (%)
		Lon	Lat		
Vung Tau	Vietnam	107.1° E	10.3° N	Oct 2018–Mar 2023	9.20
Quarry Bay	China	114.2° E	22.3° N	Oct 2018–Dec 2024	0.31
Currimao	Philippines	120.5° E	18.0° N	Oct 2018–Dec 2024	16.42
Ishigaki	Japan	124.2° E	24.3° N	Oct 2018–Dec 2024	0.28
Manila	Philippines	121.0° E	14.6° N	Oct 2018–Dec 2024	6.84
Bitung	Indonesia	125.2° E	1.4° N	Oct 2018–Dec 2024	12.77
Nagasaki	Japan	130.0° E	32.7° N	Oct 2018–Dec 2024	0.35
Nakano Sima	Japan	129.9° E	29.8° N	Oct 2018–Dec 2024	8.95
Naze	Japan	129.5° E	28.4° N	Oct 2018–Dec 2024	9.00
Hamada	Japan	132.1° E	34.9° N	Oct 2018–Dec 2024	0.31
Aburatsu	Japan	131.4° E	31.6° N	Oct 2018–Dec 2024	0.35
Nishinoomote	Japan	131.0° E	30.7° N	Oct 2018–Dec 2024	9.60
Toyama	Japan	137.2° E	36.8° N	Oct 2018–Mar 2023	0.10
Maisaka	Japan	137.6° E	34.7° N	Oct 2018–Dec 2024	0.31
Kushimoto	Japan	135.8° E	33.5° N	Oct 2018–Dec 2024	0.30

Table 2. *Cont.*

Tide Gauge	Country	Location		Time Period	Missing Percentage (%)
		Lon	Lat		
Yakutat	USA	139.7° W	59.5° N	Oct 2018–Dec 2024	1.98
Sitka	USA	135.3° W	57.1° N	Oct 2018–Dec 2024	0.25
Ketchikan	USA	131.6° W	55.3° N	Oct 2018–Dec 2024	0.18
Tofino	Canada	125.9° W	49.2° N	Oct 2018–Dec 2024	0.03
Bamfield	Canada	125.1° W	48.8° N	Oct 2018–Dec 2024	0.03
Neah Bay	USA	124.6° W	48.4° N	Oct 2018–Dec 2024	0.48
South Beach	USA	124.0° W	44.6° N	Oct 2018–Dec 2024	3.93
Crescent	USA	124.2° W	41.7° N	Oct 2018–Dec 2024	0.09
San Francisco	USA	122.5° W	37.8° N	Oct 2018–Dec 2024	2.07
La Jolla	USA	117.3° W	32.9° N	Oct 2018–Dec 2024	0.14

3.2. Altimeter SLA

The altimetry *SLA* is calculated as,

$$SLA = Altitude - Range - Corrections - MSS \quad (1)$$

where the *Altitude* represents the distance between the satellite's center of mass and the reference ellipsoid (i.e., the WGS84 ellipsoid), the *Range* gives the height of the satellite above the earth surface. *Corrections* include range and geophysical corrections, and the *MSS* is the interpolated values from the 2023 Hybrid MSS model, which is computed over the 1993–2012 period using data from multiple satellite altimeters [38]. Table 3 lists the corrections used in this study, including dynamic atmospheric correction (DAC) and geocentric ocean tide corrections, which are considered the optimal corrections through our test. As for Sentinel-3A, for instance, the wet tropospheric correction (WTC) provided by the GPD+ algorithm was chosen over the correction derived from the onboard microwave radiometer (MWR), as the GPD+ algorithm combines effective measurements from MWR, GNSS coastal and inland stations, and scanning imaging MWR [10]. Similarly, the Global Ionosphere Maps (GIM) model is used for the ionospheric correction, replacing the dual-frequency SRAL ionospheric correction, as interpretation of dual-band measurements can be unreliable around the coast [9]. Additionally, consistency when comparing missions, we replaced the geocentric ocean tide corrections of Sentinel-3A and ICESat-2 with those from the FES2022 model, the same model used for SWOT.

Table 3. Sources of corrections applied to altimeter-derived SLA measurements.

Mission	Sentinel-3A	ICESat-2	SWOT
Dry tropospheric correction	ECMWF	NASA GMAO GEOS-5	ECMWF
Wet tropospheric correction	GPD+	NASA GMAO GEOS-5	ECMWF
Ionospheric correction	GIM	NASA GMAO GEOS-5	GIM
Dynamic atmospheric correction	MOG2D	MOG2D	MOG2D
Geocentric ocean tide correction	FES2022	FES2022	FES2022
Solid Earth tide	Cartwright and Tayler (1971) [39]; Cartwright and Edden (1973) [40]	IERS Conventions (2010) [41]	Cartwright and Tayler (1971) [39] Cartwright and Edden (1973) [40]

Table 3. *Cont.*

Mission	Sentinel-3A	ICESat-2	SWOT
Pole tide	Wahr (1985) [42]	IERS Conventions (2010) [41]	Desai, Wahr, and Beckley (2015) [43]
Mean sea surface	2023 Hybrid [38]	2023 Hybrid [38]	2023 Hybrid [38]

3.3. Tide Gauge SLA

The tide gauge SSH records are processed using an outlier removal criterion based on the official guideline [44]. To achieve this, the median value and the 90th percentile value of the SSH observations are first calculated, and the SSH values that deviate from the median by more than three times the absolute difference between the 90th percentile and the median are considered as outliers. The *SLA* estimates from tide gauge data are computed using the following equations,

$$SLA_{tg} = SSH - DAC - Ocean\ Tide - MSL \quad (2)$$

where the *DAC* is obtained by interpolating the values provided by the two-dimensional Gravity Waves (MOG2D) model to the exact time and location of the tide gauge data. The tide corrections are calculated using the unified tidal analysis and prediction method [45], which is designed to process multi-year records with irregular temporal sampling. The *MSL* is defined as the mean value of the tide gauge measurements over the study period from October 2018 to December 2024. To ensure temporal alignment with satellite observations, the hourly tide gauge data are interpolated to match the altimeter time stamps using a nearest-neighbor interpolation method, ensuring that the time difference between tide gauge and nearby altimeter measurements is kept within 30 min.

3.4. Validation of Altimeter Data Using Tide Gauge Data

Altimeter observations located within 50 km from the coastline are utilized for validation. To reduce the impact of the different spatial resolutions achieved by different altimeters, the spatial and temporal collocation with tide gauge data with a 134 km spatial radius and a 30 min time window is conducted. The selection of 134 km is a trade-off between retaining the correlation between altimeter data and tide gauge records and achieving sufficient altimeter data for average [6]. Then, a two-step outlier removal strategy was applied to altimeter data. First, any *SLA* values exceeding ±1 m are discarded. Second, a 3σ threshold filter is applied to the *SLA* time series to remove *SLA* values beyond the 99.7% confidence interval.

To remove the reference offset caused by the mismatch between the tide gauge MSL period and the 2023 Hybrid MSS realization period, the mean *SLA* of each dataset is subtracted before calculating the statistical metrics. Subsequently, all valid collocations are used to calculate four statistical metrics to assess the agreement between altimetry and tide gauge data, which are bias, root mean square error (RMSE), correlation coefficient (R) and the number of collocated points, which can be obtained as follows,

$$Bias = \frac{1}{N}\sum_{i=1}^{N}(S(i) - S_0(i)) \quad (3)$$

$$RMSE = \sqrt{\frac{1}{N}\sum_{i=1}^{N}(S(i) - S_0(i))^2} \quad (4)$$

$$R = \frac{\sum_{i=1}^{N}[(S(i) - \overline{S})(S_0(i) - \overline{S_0})]}{\sqrt{\sum_{i=1}^{N}(S(i) - \overline{S})^2 \sum_{i=1}^{N}(S_0(i) - \overline{S_0})^2}} \quad (5)$$

where S and S_0 represent the altimeter observations and the tide gauge measurements at the collocated point, respectively. N is the total number of valid collocated points. $\overline{S}$ and $\overline{S_0}$ denote the mean values of the altimeter and tide gauge data. Finally, scatterplots and Taylor diagrams are plotted to visualize the results and used to compare the consistency between different altimeters and tide gauge observations.

3.5. Triple Collocation Functional Relationship (FR) Model

Although tide gauge observations are commonly used for validating satellite altimeter data, they are subject to VLM and local environmental variability, which may introduce significant uncertainties into long-term trends. Therefore, the triple collocation statistical method is also adopted to quantify both the systematic and random errors of each dataset, including altimeters and tide gauges, without assuming the tide gauge data as the ground truth [46].

To reduce the impact of the different spatial resolutions achieved by different altimeters, the satellite super observations are first constructed by averaging observations within a time window of 30 s for Sentinel-3A and 25 s for ICESat-2 and SWOT. Then, the super observations from these three data sources are collocated in space and time, with a temporal threshold of 6 h and a spatial radius threshold of 1°. When collocating tide gauge and satellite data, we select satellite observations located within a 1.5° × 1.5° latitude-longitude region centered at each tide gauge station. Within this spatial window, super observations are constructed. Super observations are then collocated in space and time, and the hourly tide gauge data are linearly interpolated to the timestamp of each matched satellite pair to ensure that the time difference between tide gauge measurements and altimeter observations is within 30 min. Finally, for each collocation we employ a functional relationship (FR) model, which assumes that three independent datasets (denoted as x, y, and z) are linearly related to a fixed but unknown true value T [46]. Each dataset contains its random error component, and these errors are assumed to be mutually independent. The relationship is expressed as,

$$x = T + e_x \tag{6}$$

$$y = \alpha_1 + \beta_1 T + e_y \tag{7}$$

$$z = \alpha_2 + \beta_2 T + e_z \tag{8}$$

and the goal is to estimate the unknown parameters α_1, β_1, α_2, β_2, along with the variances of the random errors e_x, e_y. The parameters β_1, β_2 are computed as follows,

$$\beta_1 = <y^* z^*> \; / \; <x^* z^*> \tag{9}$$

$$\beta_2 = <y^* z^*> \; / \; <x^* y^*> \tag{10}$$

where $<\cdot>$ indicates the sample mean of the enclosed quantity and x^*, y^*, z^* are obtained by subtracting the respective means from the original variables x, y, z. Once β_1 and β_2 are known, the systematic deviation α_1 and α_2 can be obtained,

$$\alpha_1 = < y > - \beta_1 < x > \tag{11}$$

$$\alpha_2 = < z > - \beta_2 < x > \tag{12}$$

Based on the above expressions, we can quantify the relationship between y and z using,

$$Y = \alpha_3 + \beta_3 Z \tag{13}$$

$$\alpha_3 = \alpha_1 - \alpha_2 \beta_3 \tag{14}$$

$$\beta_3 = \beta_1/\beta_2 \tag{15}$$

Using Equations (9) and (10), the variances of the random errors are subsequently derived as,

$$< e_X^2 > = < x^{*2} > - < x^* y^* > < x^* z^* > / < y^* z^* > \tag{16}$$

$$< e_y^2 > = < y^{*2} > - < x^* y^* > < y^* z^* > / < x^* z^* > \tag{17}$$

$$< e_z^2 > = < z^{*2} > - < x^* z^* > < y^* z^* > / < x^* y^* > \tag{18}$$

The above equations are based on the method described in [46]. Notably, the outcome of this method is invariant with respect to which dataset is chosen to be x, y, or z. After estimating the model parameters (e.g., α_1, α_2, β_1, β_2) and calculating the variance of random errors for each collocation, the bootstrap method with 200 resampling iterations is utilized to obtain the standard error $\hat{S}_B(\hat{\theta})$ and form 95% confidence interval for each model parameters, which is determined as $\hat{\theta} \pm 1.96 \times \hat{S}_B(\hat{\theta})$ [46].

All data processing and statistical analyses are preformed using Python (version 3.11). The main packages used in this study include NumPy (version 1.26), Matplotlib (version 3.10), SciPy (version 1.15), Pandas (version 2.2.3), and GeoPandas (version 1.1). The topographic and bathymetric maps were produced using GMT (version 6.5).

4. Results

4.1. Comparison of Altimeter SLA Estimates Against Tide Gauge Measurements

To assess the agreement between point-wise satellite observations and tide gauge records in the two selected study areas, we first generate Taylor diagrams to compare altimetry-derived *SLA* estimates with values from tide gauges. The Taylor diagram offers a concise statistical framework for displaying three key metrics, which are the correlation coefficient, the centered root-mean-square difference (RMSE), and the standard deviation (STD). In this experiment, tide gauge measurements serve as the reference dataset, while the altimeter data are treated as the test dataset. Figure 3 presents Taylor diagrams of *SLA* in the coastal region of East Asia over four coastal zones: 0–5 km, 5–10 km, 10–20 km, and 20–50 km, respectively. In the nearshore zone (0–5 km, Figure 3a), SWOT demonstrates the best agreement with tide gauge observations, exhibiting both the lowest STD (0.14 m) and RMSE (0.06 m) among the three altimeters, as well as a strong correlation (0.73). This highlights SWOT's strong potential in capturing high-resolution coastal sea level variations. ICESat-2 also performs well, with a correlation of 0.70 and an RMSE of 0.09 m. In contrast, Sentinel-3A shows the worst performance in this zone, which may be due to its larger footprint in the across-track direction. Its STD reaches 0.16 m, and the correlation with tide gauges is only 0.63. As the offshore distance increases, the performance of all three altimeters gradually improves. In the 5–50 km zone (Figure 4b–d), all three altimeters show reduced variability and stronger correlations (>0.75), with RMSE values dropping below 0.07 m, suggesting that the impact of coastal complexity on altimetric observations becomes less significant farther from shore.

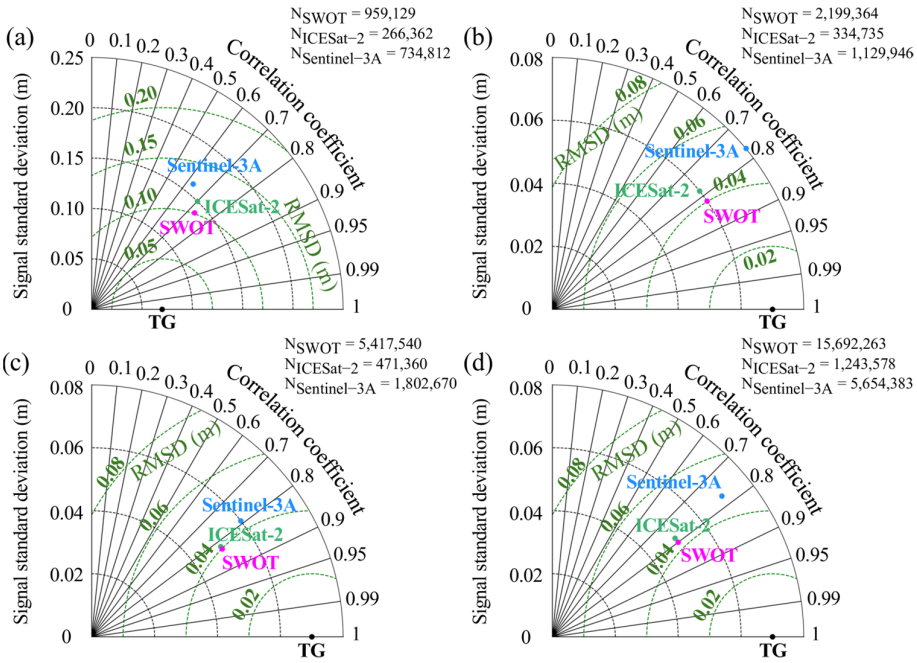


Figure 3. Taylor diagrams comparing altimeter-derived SLA estimates with tide gauge SLA across four coastal zones in study area 1 (the coastal region of East Asia): (**a**) 0–5 km, (**b**) 5–10 km, (**c**) 10–20 km, and (**d**) 20–50 km.

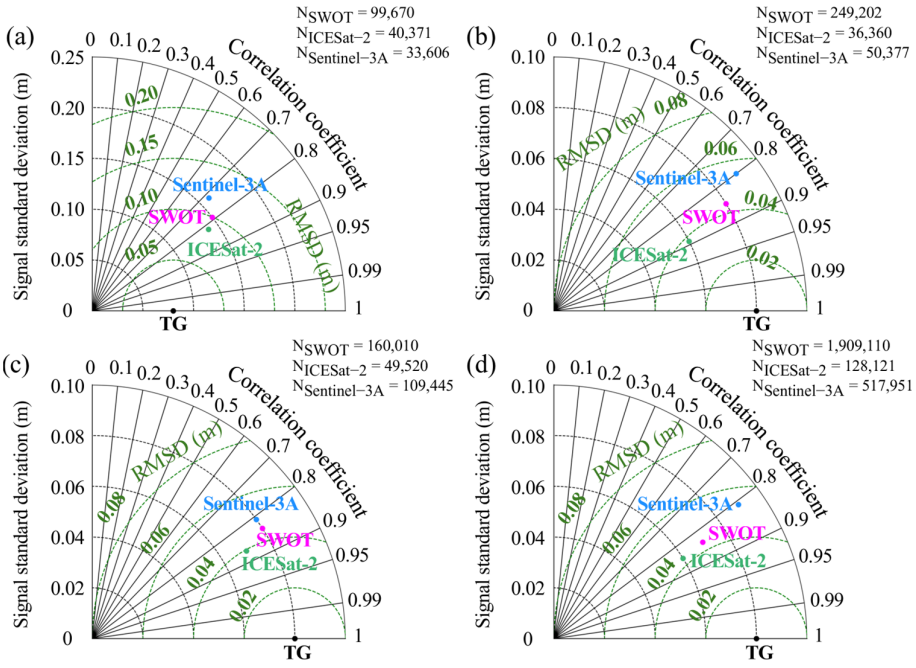


Figure 4. Taylor diagrams comparing altimeter-derived SLA estimates with tide gauge SLA across four coastal zones in study area 2 (the US West Coast): (**a**) 0–5 km, (**b**) 5–10 km, (**c**) 10–20 km, and (**d**) 20–50 km.

In the US West Coast, a similar validation analysis is conducted. The results exhibit characteristics similar to those observed in the coastal region of East Asia, and this region demonstrates generally higher consistency between altimeter and tide gauge *SLA* (Figure 4). Specifically, in the 0–5 km and 5–50 km coastal zones, the correlation coefficients between each altimeter and tide gauge records vary within the following ranges (i.e., 0.72–0.81 for Sentinel-3A, 0.82–0.85 for ICESat-2, and 0.79–0.84 for SWOT). Among them, the ICESat-2 demonstrates the best performance in this region. Particularly, in the 0–5 km zone,

the ICESat-2 achieves a correlation of 0.82 with tide gauge measurements, surpassing both SWOT (0.79) and Sentinel-3A (0.72). In terms of RMSE, the ICESat-2 also performs the best (0.10 m) when compared to the SWOT (0.11 m) and Sentinel-3A (0.14 m). This superiority is likely due to ICESat-2's reduced range bias error at higher latitudes, where more frequent crossover observations enhance measurement reliability. Although the SWOT also benefits from its wide-swath geometry and denser crossover coverage at higher latitudes, its observability degrades to 30–45 km at high latitudes due to SWH-induced instrument noise. These effects may partially explain the inferior performance of SWOT in high-latitude coastal regions when compared to the ICESat-2 [47]. Nevertheless, the results also confirm the strong capability of the SWOT in capturing coastal sea level signals, supporting its application in nearshore altimetry.

To further examine the linear relationship between satellite altimeter and tide gauge measurements, we perform the orthogonal regression analysis (also known as major axis regression) for each tide gauge across four coastal zones. As a representative case, the Hamada station is selected due to its location toward the open ocean and close to the continental shelf break—conditions that strongly influence the correlation between satellite and tide gauge data, making it suitable for illustrative analysis. Figure 5 presents scatterplots of *SLA* for Sentinel-3A, ICESat-2, and SWOT at the Hamada station. Each panel includes a red line representing the fitted orthogonal regression line, with a black dashed line denoting the 1:1 reference line, and key statistical metrics (i.e., Bias, RMSE, Correlation coefficient, and the number of collocations). Across all subplots, the satellite-derived values exhibit strong linear relationships with tide gauge data, which confirms their consistency with each other. Nevertheless, the regression slopes being consistently below 1 indicate that the satellite altimeters tend to underestimate *SLA* when compared to in situ measurements. In addition to this representative case, all point-wise validation results for SWOT in both study areas are summarized in Tables 4 and 5.

Table 4. Point-wise validation results of SWOT-derived SLA against tide gauge records in the coastal region of East Asia over the 0–5 km and 5–10 km distance bands.

TG	0–5 km			5–10 km		
	RMSE (m)	**Corr**	**Number**	**RMSE (m)**	**Corr**	**Number**
Aburatsu	0.06	0.74	89	0.05	0.81	97
Bitung	0.05	0.70	65	0.04	0.80	81
Currimao	0.08	0.65	58	0.06	0.78	63
Hamada	0.07	0.75	159	0.06	0.84	162
Ishigaki	0.06	0.76	84	0.05	0.87	113
Kushimot	0.07	0.72	108	0.05	0.79	114
Maisaka	0.06	0.76	108	0.04	0.83	124
Manila	0.07	0.70	67	0.05	0.78	68
Nagasaki	0.06	0.72	88	0.05	0.85	105
Nakano	0.06	0.73	87	0.05	0.82	116
Naze	0.07	0.68	72	0.05	0.80	103
Nishinoo	0.07	0.71	78	0.05	0.79	88
QuarryBay	0.06	0.82	106	0.05	0.84	110

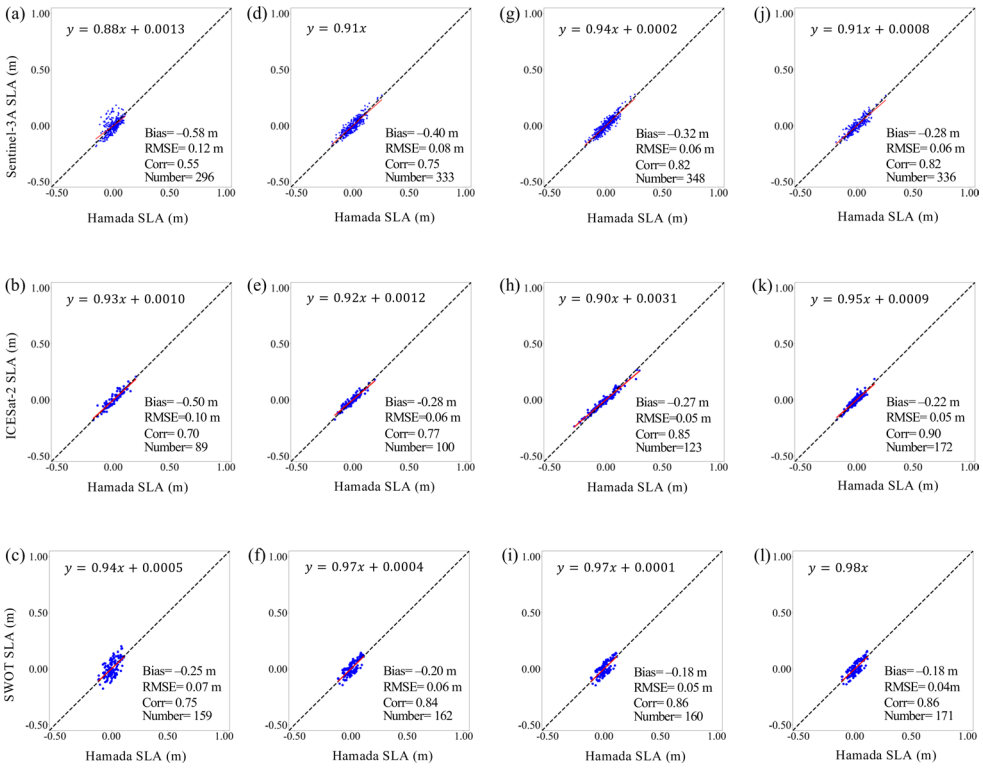


Figure 5. Scatter plots of SLA between the altimeter and the Hamada tide gauge station. Each column represents a different coastal zone: (**a**–**c**) 0–5 km, (**d**–**f**) 5–10 km, (**g**–**i**) 10–20 km, and (**j**–**l**) 20–50 km. Rows correspond to the three altimeters: Sentinel-3A (**top**), ICESat-2 (**middle**), and SWOT (**bottom**). The red line represents the linear regression between the two datasets, and the black dash line depicts the ideal relationship, indicating the perfect agreement between the altimeter and tide gauge data.

Table 5. Point-wise validation results of SWOT-derived SLA against tide gauge records in the US West Coast over the 0–5 km and 5–10 km distance bands.

TG	0–5 km			5–10 km		
	RMSE (m)	Corr	Number	RMSE (m)	Corr	Number
Yakutat	0.07	0.75	91	0.05	0.92	201
Sitka	0.07	0.84	303	0.06	0.87	300
Ketchika	0.08	0.78	306	0.06	0.85	310
Tofino	0.06	0.83	230	0.06	0.86	236
Bamfield	0.07	0.79	195	0.06	0.86	228
Neah Bay	0.06	0.82	207	0.05	0.83	200
South Beach	0.05	0.75	93	0.05	0.79	109
Crescent	0.08	0.67	155	0.07	0.72	179
San Francisco	0.06	0.83	144	0.05	0.90	181
La Jolla	0.05	0.85	137	0.04	0.90	176

These results further demonstrate the consistent performance of the SWOT mission in nearshore environments. In both study regions, the differences between the 0–5 km and 5–10 km coastal zones are relatively small. Specifically, the bias values remain within −0.35 m to −0.20 m for the 0–5 km coastal zone and −0.30 m to −0.15 m for the 5–10 km coastal zone. The RMSE values also remain stable, generally ranging from 0.04 m to 0.08 m. This consistency across different distances to coasts reinforces the superiority of SWOT-derived *SLA* observations in capturing nearshore sea level variations.

4.2. Evaluation of Altimeter and Tide Gauge Errors Using the Triple Collocation FR Model

To further validate the altimeter's performance, we use the triple collocation functional relationship (FR) model under the assumption that the random errors of each dataset are mutually independent. Figure 6 presents the scatter diagrams of the results in the coastal region of the East Asia, which is based on the satellite *SLA* observations within 50 km from the coast. Four columns of triple collocation results are presented, each of them involves a different combination of three datasets and provides the number of collocations (n), the variance of random errors (var) for the two datasets involved in the comparison, and the FR regression equation.

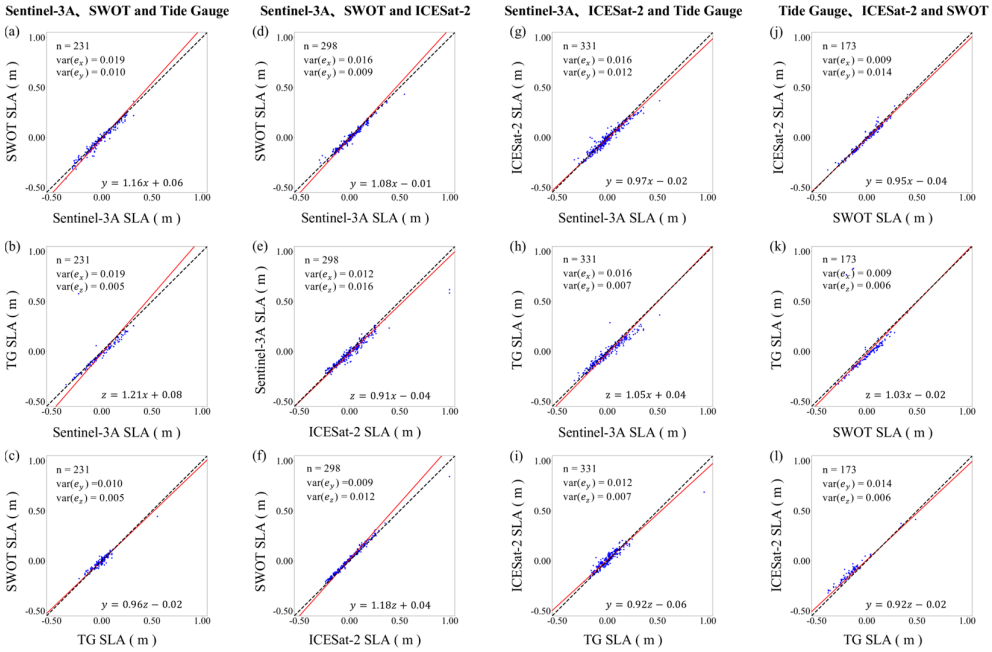


Figure 6. Scatter diagrams with estimated FR lines from the triple collocation results of SLA in the coastal region of East Asia. Each panel shows the comparison between two datasets, with associated random error variances and the number of collocations. Panels (**a**–**c**) Sentinel-3A, SWOT, and tide gauge; (**d**–**f**) Sentinel-3A, SWOT, and ICESat-2; (**g**–**i**) Sentinel-3A, ICESat-2, and tide gauge; (**j**–**l**) tide gauge, ICESat-2, and SWOT. The red line represents the linear regression between the two datasets, and the black dash line depicts the ideal relationship.

The first group combines Sentinel-3A, SWOT, and tide gauge data over the period of July 2023 and December 2024. The scatter plots show that when values are high, the Sentinel-3A gives an underestimation of *SLA*. In addition, its variance of the random errors is the largest among the three (0.019 m^2), while SWOT and tide gauge data show better consistency ($Y = -0.02 + 0.96 * Z$) with smaller error variances of 0.010 m^2 and 0.005 m^2, respectively. The second and third columns (Figure 6d–i) assess the performance of Sentinel-3A, SWOT, and ICESat-2, as well as Sentinel-3A, ICESat-2, and tide gauge datasets, covering the available time periods for each data source. As shown in the graph, Sentinel-3A and ICESat-2 show a tendency to underestimate higher *SLA* values, which may be attributed to differences in their applied corrections and respective altimetry techniques. Comparing the scatterplots across the first three groups, it is evident that combinations excluding Sentinel-3A exhibit tighter clustering of points around the red regression line, whereas those including Sentinel-3A appear more dispersed. This further supports the finding that Sentinel-3A's nearshore data quality is more susceptible to land contamination, which is due to its larger footprint in the across-track direction. The fourth group (Figure 6j–l), which includes ICESat-2, SWOT, and tide gauge data, demonstrates the

strongest internal consistency, with points closely aligned to the regression lines and low error variances for all three datasets (TG = 0.006 m^2, SWOT = 0.009 m^2, ICESat-2 = 0.014 m^2), indicating SWOT's ability to provide reliable *SLA* estimates in the study regions. Finally, Table 6 summarizes the estimated parameters and corresponding 95% confidence intervals, which is calculated using a bootstrap resampling method. A key finding is that the variance of the random errors associated with Sentinel-3A is significantly higher than that of the other data sources. In contrast, SWOT exhibits error variances more comparable to those of tide gauge records. This is consistent with the scatter diagrams shown in Figure 6, where the SWOT-derived *SLA* aligns more closely with in situ measurements. Moreover, the confidence intervals associated with SWOT are generally narrower than those of the other altimeters, suggesting more stable and concentrated error characteristics, and further supporting the reliability of SWOT in nearshore applications.

Table 6. Triple collocation results for the coastal region of East Asia. Values in parentheses indicate the 95% confidence intervals.

Datasets (x, y, z)	n	$<x>$ (m)	$<e_x^2>$ (m^2)	$<e_y^2>$ (m^2)	$<e_z^2>$ (m^2)
S3A, SWOT and TG	231	−0.57	0.019 (0.016, 0.023)	0.010 (0.009, 0.010)	0.005 (0.004, 0.005)
S3A, SWOT and IS2	298	−0.66	0.016 (0.015, 0.020)	0.009 (0.008, 0.010)	0.012 (0.009, 0.014)
S3A, IS2 and TG	331	−0.60	0.016 (0.012, 0.019)	0.012 (0.011, 0.013)	0.007 (0.006, 0.007)
SWOT, IS2 and TG	173	−0.59	0.009 (0.007, 0.011)	0.014 (0.012, 0.016)	0.006 (0.006, 0.006)

Furthermore, Figure 7 and Table 7 summarize the results in the US West Coast. Compared with the coastal region of East Asia, the number of valid collocations in this area is lower across all groups, which may be due to fewer matched satellite and tide gauge data within the defined 134 km spatial radius and 30 min temporal window. In addition, the mean *SLA* values of the x-variable in each group are slightly lower than those in the coastal region of East Asia, which reflects the spatial differences in *SLA* distribution between these two study areas. As shown, the results in Table 7 are broadly consistent with those in Table 6. Among the three altimeters, the ICESat-2 consistently exhibits the lowest random error variance across all combinations, with narrower confidence intervals when compared to the Sentinel-3A and SWOT, which indicates more consistent and reliable measurement quality. This supports the earlier findings that the ICESat-2, due to its smaller footprint, is capable of delivering more accurate and consistent *SLA* estimates in mid- to high-latitude coastal environments.

Table 7. Triple collocation results for the US West Coast. Values in parentheses indicate the 95% confidence intervals.

Datasets (x, y, z)	n	$<x>$ (m)	$<e_x^2>$ (m^2)	$<e_y^2>$ (m^2)	$<e_z^2>$ (m^2)
S3A, SWOT and TG	148	−0.66	0.015 (0.013, 0.017)	0.010 (0.008, 0.012)	0.007 (0.006, 0.008)
S3A, SWOT and IS2	232	−0.64	0.017 (0.014, 0.020)	0.007 (0.005, 0.009)	0.007 (0.005, 0.008)
S3A, IS2 and TG	169	−0.73	0.015 (0.012, 0.018)	0.007 (0.005, 0.008)	0.004 (0.003, 0.005)
SWOT, IS2 and TG	169	−0.61	0.009 (0.006, 0.011)	0.006 (0.005, 0.007)	0.004 (0.002, 0.004)

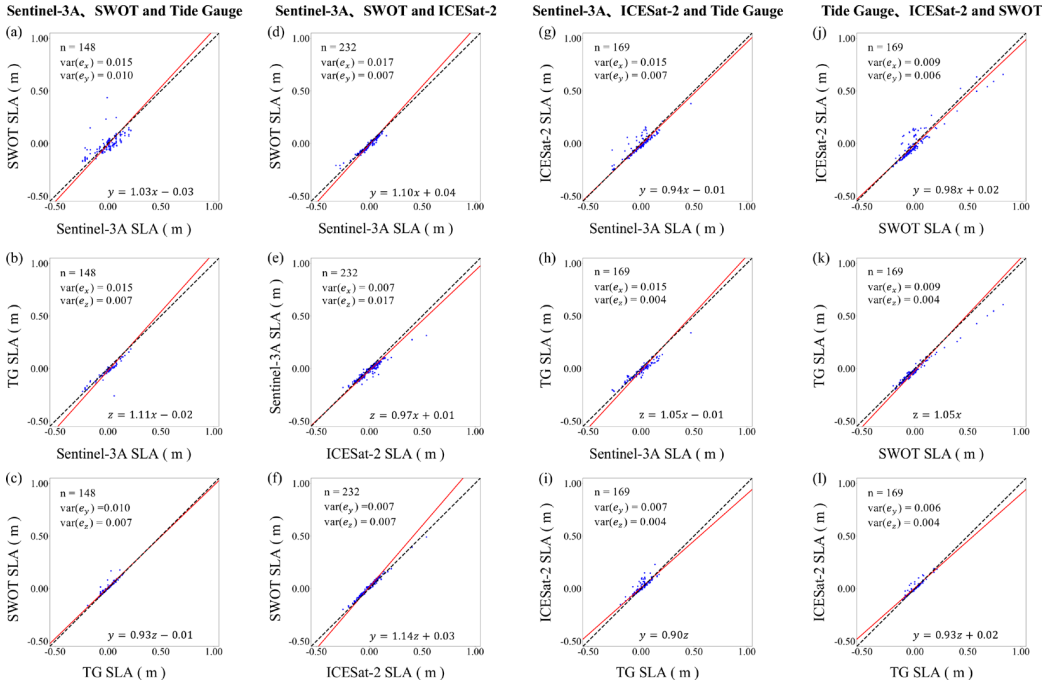


Figure 7. Scatter diagrams with estimated FR lines from the triple collocation results of SLA in the US West Coast. Each panel shows the comparison between two datasets, with associated random error variances and the number of collocations. Panels (**a**–**c**) Sentinel-3A, SWOT, and tide gauge; (**d**–**f**) Sentinel-3A, SWOT, and ICESat-2; (**g**–**i**) Sentinel-3A, ICESat-2, and tide gauge; (**j**–**l**) tide gauge, ICESat-2, and SWOT. The red line represents the linear regression between the two datasets, and the black dash line depicts the ideal relationship.

5. Conclusions

In this study, we evaluate the performance of the SWOT mission in measuring *SLA* estimates with respect to the 2023 hybrid mean sea surface across two coastal regions (i.e., the coastal region of East Asia and the US West Coast). We first validate the altimeter data using tide gauge observations over four coastal zones (i.e., 0–5 km, 5–10 km, 10–20 km, and 20–50 km). The results show that the SWOT consistently demonstrates strong agreement with in situ tide gauge data. In the coastal region of the East Asia, it achieves the lowest STD (0.14 m) and RMSE (0.06 m) in the 0–5 km zone, highlighting its capability to capture nearshore sea surface heights with high accuracy. In comparison, the Sentinel-3A exhibited larger variability and weaker consistency with tide gauges (STD = 0.16 m, RMSE = 0.12 m), mainly due to its large footprint in the across-track direction, which makes its return waveforms more susceptible to land contamination and distortion [16,48]. In the US West Coast, the ICESat-2 outperforms other altimeters, achieving the highest correlation (0.82) and lowest RMSE (0.08 m) in the 0–5 km zone, which may be attributed to its denser crossover observations and reduced range bias at higher latitudes [17]. The SWOT shows stable and favorable performance in the 0–5 km coastal zone in both study areas, with RMSE and correlation values (0.06 m/0.73 for the coastal region of East Asia, 0.11 m/0.79 for the US West Coast), maintaining good consistency with tide gauge data.

Based on the validated linear relationships and the assumption of mutually independent errors among these datasets, the triple collocation functional relationship model is used to further evaluate the performance of the three altimeters and tide gauge data. The results show quantitative estimates of both systematic errors and the variance of random errors for each dataset, along with their confidence intervals. As expected, the scatter diagrams involving Sentinel-3A show more dispersed points around the fitted regression line, indicating larger uncertainties. Meanwhile, the estimated random error variances

for the SWOT are half of those for the Sentinel-3A (e.g., 0.009 m^2 vs. 0.019 m^2) with its superior stability in observations near coasts. Another noteworthy point is the consistent underestimation of high *SLA* values by both Sentinel-3A and ICESat-2, and this may be due to the differences in their applied corrections or inherent characteristics of their altimetric instruments, which require further investigation in our future work.

Author Contributions: H.Z.: Software: Formal analysis, and Writing—original draft. F.P.: Supervision, Writing—review & editing, and Conceptualization. Y.S.: Supervision, Writing—review & editing, and Conceptualization. All authors have read and agreed to the published version of the manuscript.

Funding: This research is supported by the National Natural Science Foundation of China (grant No. 42474022 and 42106175) and Natural Science Foundation of Guangdong Province (grant No. 2022A1515011299).

Data Availability Statement: The original contributions presented in this study are included in the article. Further inquiries can be directed to the corresponding author.

Acknowledgments: The authors would like to sincerely thank EUMETSAT, NSIDC, AVISO+, and the University of Hawaii Sea Level Center (UHSLC) for providing access to the Sentinel-3A NTC products, ICESat-2 ATL12 products, SWOT LR products, and hourly tide gauge records, which were essential for this study.

Conflicts of Interest: The authors declare no conflicts of interest.

References

1. Melet, A.; Almar, R.; Hemer, M.; Le Cozannet, G.; Meyssignac, B.; Ruggiero, P. Contribution of Wave Setup to Projected Coastal Sea Level Changes. *J. Geophys. Res. Ocean.* **2020**, *125*, e2020JC016078. [CrossRef]
2. Cazenave, A.; Gouzenes, Y.; Birol, F.; Leger, F.; Passaro, M.; Calafat, F.M.; Shaw, A.; Nino, F.; Legeais, J.F.; Oelsmann, J.; et al. Sea Level along the World's Coastlines Can Be Measured by a Network of Virtual Altimetry Stations. *Commun. Earth Environ.* **2022**, *3*, 117. [CrossRef]
3. Srinivasan, M.; Tsontos, V. Satellite Altimetry for Ocean and Coastal Applications: A Review. *Remote Sens.* **2023**, *15*, 3939. [CrossRef]
4. Birgiel, E.; Ellmann, A.; Delpeche-Ellmann, N. Examining the Performance of the Sentinel-3 Coastal Altimetry in the Baltic Sea Using a Regional High-Resolution Geoid Model. In Proceedings of the 2018 Baltic Geodetic Congress (BGC Geomatics), Olsztyn, Poland, 21–23 June 2018; IEEE: New York, NY, USA; pp. 196–201.
5. An, Z.; Chen, P.; Tang, F.; Yang, X.; Wang, R.; Wang, Z. Evaluating the Performance of Seven Ongoing Satellite Altimetry Missions for Measuring Inland Water Levels of the Great Lakes. *Sensors* **2022**, *22*, 9718. [CrossRef] [PubMed]
6. Vinogradov, S.V.; Ponte, R.M. Annual Cycle in Coastal Sea Level from Tide Gauges and Altimetry. *J. Geophys. Res. Ocean.* **2010**, *115*, 2009JC005767. [CrossRef]
7. Valle-Rodríguez, J.; Trasviña-Castro, A. Sea Level Anomaly Measurements from Satellite Coastal Altimetry and Tide Gauges at the Entrance of the Gulf of California. *Adv. Space Res.* **2020**, *66*, 1593–1608. [CrossRef]
8. Yang, L.; Lin, L.; Fan, L.; Liu, N.; Huang, L.; Xu, Y.; Mertikas, S.P.; Jia, Y.; Lin, M. Satellite Altimetry: Achievements and Future Trends by a Scientometrics Analysis. *Remote Sens.* **2022**, *14*, 3332. [CrossRef]
9. Handoko, E.; Fernandes, M.; Lázaro, C. Assessment of Altimetric Range and Geophysical Corrections and Mean Sea Surface Models—Impacts on Sea Level Variability around the Indonesian Seas. *Remote Sens.* **2017**, *9*, 102. [CrossRef]
10. Fernandes, M.; Lázaro, C. GPD+ Wet Tropospheric Corrections for CryoSat-2 and GFO Altimetry Missions. *Remote Sens.* **2016**, *8*, 851. [CrossRef]
11. Donlon, C.; Berruti, B.; Buongiorno, A.; Ferreira, M.-H.; Féménias, P.; Frerick, J.; Goryl, P.; Klein, U.; Laur, H.; Mavrocordatos, C.; et al. The Global Monitoring for Environment and Security (GMES) Sentinel-3 Mission. *Remote Sens. Environ.* **2012**, *120*, 37–57. [CrossRef]
12. ESA, S3 Altimetry Instruments. 2025. Available online: https://sentiwiki.copernicus.eu/web/s3-altimetry-instruments (accessed on 19 October 2025).
13. Mostafavi, M.; Delpeche-Ellmann, N.; Ellmann, A. Accurate Sea Surface Heights from Sentinel-3A and Jason-3 Retrackers by Incorporating High-Resolution Marine Geoid and Hydrodynamic Models. *J. Geod. Sci.* **2021**, *11*, 58–74. [CrossRef]

14. Santos-Ferreira, A.M.; Da Silva, J.C.B.; Magalhaes, J.M. SAR Mode Altimetry Observations of Internal Solitary Waves in the Tropical Ocean Part 1: Case Studies. *Remote Sens.* **2018**, *10*, 644. [CrossRef]
15. Yang, J.; Zhang, J.; Jia, Y.; Fan, C.; Cui, W. Validation of Sentinel-3A/3B and Jason-3 Altimeter Wind Speeds and Significant Wave Heights Using Buoy and ASCAT Data. *Remote Sens.* **2020**, *12*, 2079. [CrossRef]
16. Peng, F.; Deng, X. Validation of Sentinel-3A SAR Mode Sea Level Anomalies around the Australian Coastal Region. *Remote Sens. Environ.* **2020**, *237*, 111548. [CrossRef]
17. Neumann, T.; Brenner, A.; Hancock, D.; Robins, J.; Saba, J.; Harbeck, K.; Gibbons, A.; Lee, J.; Luthcke, S.; Rebold, T. *Ice, Cloud, and Land Elevation Satellite (ICESat-2) Project Algorithm Theoretical Basis Document (ATBD) for Global Geolocated Photons ATL03, Version 6*; NASA Goddard Space Flight Center: Greenbelt, MD, USA, 2022. [CrossRef]
18. Buzzanga, B.; Heijkoop, E.; Hamlington, B.D.; Nerem, R.S.; Gardner, A. An Assessment of Regional ICESat-2 Sea-level Trends. *Geophys. Res. Lett.* **2021**, *48*, e2020GL092327. [CrossRef]
19. Tomić, M.; Baltazar Andersen, O. ICESat-2 for Coastal MSS Determination—Evaluation in the Norwegian Coastal Zone. *Remote Sens.* **2023**, *15*, 3974. [CrossRef]
20. Neumann, T.A.; Martino, A.J.; Markus, T.; Bae, S.; Bock, M.R.; Brenner, A.C.; Brunt, K.M.; Cavanaugh, J.; Fernandes, S.T.; Hancock, D.W.; et al. The Ice, Cloud, and Land Elevation Satellite—2 Mission: A Global Geolocated Photon Product Derived from the Advanced Topographic Laser Altimeter System. *Remote Sens. Environ.* **2019**, *233*, 111325. [CrossRef]
21. Fu, L.; Pavelsky, T.; Cretaux, J.; Morrow, R.; Farrar, J.T.; Vaze, P.; Sengenes, P.; Vinogradova-Shiffer, N.; Sylvestre-Baron, A.; Picot, N.; et al. The Surface Water and Ocean Topography Mission: A Breakthrough in Radar Remote Sensing of the Ocean and Land Surface Water. *Geophys. Res. Lett.* **2024**, *51*, e2023GL107652. [CrossRef]
22. Peral, E.; Esteban-Fernández, D.; Rodríguez, E.; McWatters, D.; De Bleser, J.-W.; Ahmed, R.; Chen, A.C.; Slimko, E.; Somawardhana, R.; Knarr, K.; et al. KaRIn, the Ka-Band Radar Interferometer of the SWOT Mission: Design and in-Flight Performance. *IEEE Trans. Geosci. Remote Sens.* **2024**, *62*, 5214127. [CrossRef]
23. Vignudelli, S.; Birol, F.; Benveniste, J.; Fu, L.-L.; Picot, N.; Raynal, M.; Roinard, H. Satellite Altimetry Measurements of Sea Level in the Coastal Zone. *Surv. Geophys.* **2019**, *40*, 1319–1349. [CrossRef]
24. Montillet, J.-P.; Melbourne, T.I.; Szeliga, W.M. GPS Vertical Land Motion Corrections to Sea-level Rise Estimates in the Pacific Northwest. *J. Geophys. Res. Ocean.* **2018**, *123*, 1196–1212. [CrossRef]
25. Liu, N.; Wang, H.; Ling, T.; Feng, L. The Influence of ENSO on Sea Surface Temperature Variations in the China Seas. *Acta Oceanol. Sin.* **2013**, *32*, 21–29. [CrossRef]
26. Rong, Z.; Liu, Y.; Zong, H.; Cheng, Y. Interannual Sea Level Variability in the South China Sea and Its Response to ENSO. *Global Planet. Change* **2007**, *55*, 257–272. [CrossRef]
27. Feng, J.; Li, D.; Wang, T.; Liu, Q.; Deng, L.; Zhao, L. Acceleration of the Extreme Sea Level Rise along the Chinese Coast. *Earth Space Sci.* **2019**, *6*, 1942–1956. [CrossRef]
28. Drogoul, A.; Pannier, E.; Nguyen, M.-H.; Woillez, M.-N.; Ngo-Duc, T.; Espagne, É. Climate Change in Vietnam: Impacts and Adaptation. Available online: http://theconversation.com/climate-change-in-vietnam-impacts-and-adaptation-173462 (accessed on 14 June 2025).
29. Nakano, H.; Urakawa, S.; Sakamoto, K.; Toyoda, T.; Kawakami, Y.; Yamanaka, G. Long-Term Sea-Level Variability along the Coast of Japan during the 20th century revealed by a 1/10° OGCM. *J. Oceanogr.* **2023**, *79*, 123–143. [CrossRef]
30. Rietbroek, R.; Brunnabend, S.-E.; Kusche, J.; Schröter, J.; Dahle, C. Revisiting the Contemporary Sea-Level Budget on Global and Regional Scales. *Proc. Natl. Acad. Sci. USA* **2016**, *113*, 1504–1509. [CrossRef]
31. Yang, Z.; García-Medina, G.; Wu, W.-C.; Wang, T. Characteristics and Variability of the Nearshore Wave Resource on the U.S. West Coast. *Energy* **2020**, *203*, 117818. [CrossRef]
32. Khouakhi, A.; Villarini, G.; Zhang, W.; Slater, L.J. Seasonal Predictability of High Sea Level Frequency Using ENSO Patterns along the U.S. West Coast. *Adv. Water Resour.* **2019**, *131*, 103377. [CrossRef]
33. Sella, G.F.; Stein, S.; Dixon, T.H.; Craymer, M.; James, T.S.; Mazzotti, S.; Dokka, R.K. Observation of Glacial Isostatic Adjustment in "Stable" North America with GPS. *Geophys. Res. Lett.* **2007**, *34*, 2006GL027081. [CrossRef]
34. Lan, W.-H.; Kuo, C.-Y.; Lin, L.-C.; Kao, H.-C. Annual Sea Level Amplitude Analysis over the North Pacific Ocean Coast by Ensemble Empirical Mode Decomposition Method. *Remote Sens.* **2021**, *13*, 730. [CrossRef]
35. Fernandes, M.J.; Lázaro, C.; Vieira, T. On the Role of the Troposphere in Satellite Altimetry. *Remote Sens. Environ.* **2021**, *252*, 112149. [CrossRef]
36. Morison, J.; Hancock, D.; Dickinson, S.; Robbins, J.; Roberts, L.; Kwok, R.; Palm, S.; Smith, B.; Jasinski, M.; Plant, B.; et al. *Ice, Cloud, and Land Elevation Satellite (ICESat-2) Project Algortihm Theorectical Basis Document (ATBD) for Ocean Surface Height, Version 6*; NASA Goddard Space Flight Center: Greenbelt, MD, USA, 2022. [CrossRef]
37. Jet Propulsion Laboratory. *SWOT Science Data Products User Handbook, JPL D-109532*; Jet Propulsion Laboratory: Pasadena, CA, USA, 2024.

38. Laloue, A.; Schaeffer, P.; Pujol, M.-I.; Veillard, P.; Andersen, O.; Sandwell, D.; Delepoulle, A.; Dibarboure, G.; Faugère, Y. Merging Recent Mean Sea Surface into a 2023 Hybrid Model (from Scripps, DTU, CLS, and CNES). *Earth Space Sci.* **2025**, *12*, e2024EA003836. [CrossRef]
39. Cartwright, D.E.; Tayler, R.J. New Computations of the Tide-Generating Potential. *Geophys. J. R. Astron. Soc.* **1971**, *23*, 45–73. [CrossRef]
40. Cartwright, D.E.; Edden, A.C. Corrected Tables of Tidal Harmonics. *Geophys. J. Int.* **1973**, *33*, 253–264. [CrossRef]
41. Petit, G.; Luzum, B. (Eds.) *IERS Conventions (2010)*; IERS Technical Note No. 36; Verlag des Bundesamts für Kartographie und Geodäsie: Frankfurt am Main, Germany, 2010.
42. Wahr, J.M. Deformation Induced by Polar Motion. *J. Geophys. Res. Solid Earth* **1985**, *90*, 9363–9368. [CrossRef]
43. Desai, S.; Wahr, J.; Beckley, B. Revisiting the Pole Tide for and from Satellite Altimetry. *J. Geod.* **2015**, *89*, 1233–1243. [CrossRef]
44. Sea Level Station Monitoring Facility. Available online: http://www.iocsealevelmonitoring.org/service.php (accessed on 26 May 2025).
45. Codiga, D.L. *Unified Tidal Analysis and Prediction Using the UTide Matlab Functions*; Technical Report 2011-01; Graduate School of Oceanography, University of Rhode Island: Narragansett, RI, USA, 2011. [CrossRef]
46. Caires, S.; Sterl, A. Validation of Ocean Wind and Wave Data Using Triple Collocation. *J. Geophys. Res. Ocean.* **2003**, *108*, 2002JC001491. [CrossRef]
47. Tréboutte, A.; Carli, E.; Ballarotta, M.; Carpentier, B.; Faugère, Y.; Dibarboure, G. KaRIn Noise Reduction Using a Convolutional Neural Network for the SWOT Ocean Products. *Remote Sens.* **2023**, *15*, 2183. [CrossRef]
48. Tomić, M.; Breili, K.; Gerlach, C.; Ophaug, V. Validation of Retracked Sentinel-3 Altimetry Observations along the Norwegian Coast. *Adv. Space Res.* **2024**, *73*, 4067–4090. [CrossRef]

Disclaimer/Publisher's Note: The statements, opinions and data contained in all publications are solely those of the individual author(s) and contributor(s) and not of MDPI and/or the editor(s). MDPI and/or the editor(s) disclaim responsibility for any injury to people or property resulting from any ideas, methods, instructions or products referred to in the content.